Grazing Incidence X-ray Scattering Studies of Thin Films of an Aromatic Polyimide

Bradford J. Factor†

Department of Applied Physics, Stanford University, Stanford, California 94305

Thomas P. Russell* **and Michael F. Toney**

IBM Research Division, Almaden Research Center, 650 Harry Road, San Jose, California 95120-6099

Received November 6, 1992; Revised Manuscript Received January 27, 1993

ABSTRACT: We report grazing incidence X-ray scattering measurements of the near surface structure of an aromatic polyimide, poly(pyromellitic dianhydride–oxydianiline) (PMDA–ODA). The structure parallel to the film surface was investigated as a function of thermal treatment and film thickness. By variation of the X-ray incidence angle, the X-ray penetration into the polymer was changed from ~50 Å (surface sensitive) to the polymer film thickness, and the PMDA–ODA structure was studied as a function of this penetration depth. For thick films (≃2500 Å), we found that near the air surface the PMDA–ODA was more ordered than in the bulk of the specimen, and for thermal treatments above 300 °C, a crystalline-like ordering was observed. In the near surface region the PMDA–ODA molecules locally assumed a more planar zigzag conformation. However, the interchain packing, i.e., the coherence of order normal to the chain axis, was markedly improved. Studies of 100-Å-thick films showed that these had a crystalline-like structure comparable to that seen near the surface of the thick films. Investigations were also performed on films ~400 Å thick where the structure near the air and substrate interfaces could be assessed. While crystalline-like ordering was found near the air surface, no such ordering was evident near the substrate interface.

Introduction

The structure of polymers near surfaces and interfaces is of fundamental scientific and technological importance. The presence of an interface places restrictions on the conformations of these long chain molecules, and consequently, the spatial distribution of the polymer segments near the interface can be altered.[1-3] The surface structure of nonpolymeric materials in solid, liquid, and liquid crystalline states has been widely investigated[4] and contrasted to the bulk structure. However, owing to the connectivity of the polymer segments, the presence of a surface should have a different effect on the surface structure of polymers than in small molecule analogs.

The static surface behavior of polymers has been studied using a variety of methods which, in most cases, can be classified as either imaging or depth profiling techniques. Imaging techniques include optical and electron microscopy and, more recently, scanning tunneling and atomic force microscopy. For example, using electron microscopy, Martin et al.[5] reported the surface structure of polyimide polymers in thin droplets and observed ordered domains. However, imaging methods have a limited ability to provide information on the structure as a function of depth. To obtain depth sensitivity, depth profiling techniques are used and have been the subject of several recent reviews.[6,7] These methods include X-ray and neutron reflectivity,[6] X-ray photoelectron spectroscopy (XPS),[8] dynamic secondary ion mass spectroscopy (SIMS),[9] X-ray evanescent wave induced fluorescence,[10] and Rutherford back-scattering or forward recoil spectroscopy.[11] Of these, only X-ray and neutron reflectivity can provide structural information, and then only perpendicular to the surface.

By contrast, grazing incidence X-ray scattering (GIXS) has the ability to distinguish the surface from the bulk and provides information about structure parallel to the surface. This was the primary motivation for employing GIXS on polymers. In GIXS, the penetration depth of the X-rays impinging on a flat surface is varied from 50 Å to microns. As a result, GIXS has been employed in several studies where bulk and surface structures are compared. These include studies of elemental crystalline solids,[12,13] elemental liquids,[14] polycrystalline oxides,[15] and crystalline alloys.[16,17] Herein, a GIXS study of an aromatic polyimide is presented where it is shown that the structure of the polymer near an air interface is markedly enhanced over that found in the bulk.[18,19]

Experimental Section

The polymer investigated was poly(pyromellitic dianhydride–oxydianaline), denoted PMDA–ODA, formed by the cycloimidization of the corresponding poly(amic acid) (PAA) and/or poly(amic acid ethyl ester) (PAE). The former can only be obtained as an equimolar mixture of the meta (*m*-PAE) and para (*p*-PAE) isomers, while with the latter either pure meta or para isomers can be prepared.[20] Herein, only the results on *p*-PAE will be treated. A schematic diagram of PMDA–ODA and the unit cell are shown below.

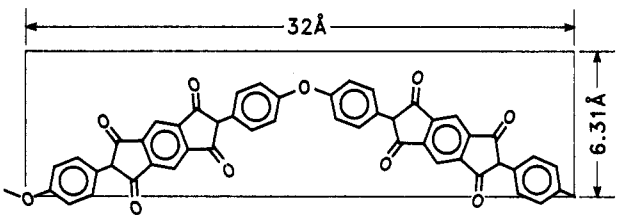

Specimens were prepared by spin coating filtered (1–5 μm) solutions of the precursor polymer in *N*-methylpyrrolidinone (NMP) onto polished silicon substrates 7.5 cm in diameter by 5 mm thick. Before use, the substrates were soaked in Chromerge for 24 h, thoroughly rinsed in deionized water, degreased in isopropyl alcohol vapors, and dried. Dewetting of the polymer solution on the substrate was avoided by etching the SiO_2 layer from the surface in a buffered HF solution (Buffered OxideEtch, Low Sodium (MOS) Electronic Grade, 6 NH_2F:1 HF). Spin coating was done at 500 rpm for ~10 s to spread the solution over

† Present address: Institut Curie, Section Physique et Chimie, 75005 Paris, France.

0024-9297/93/2226-2847$04.00/0

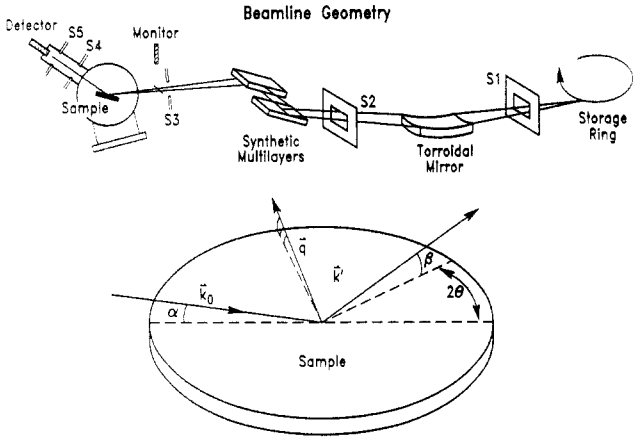

Figure 1. Schematic diagram of the beamline geometry (top) and the geometry of the incident and scattered beams at the sample (bottom).

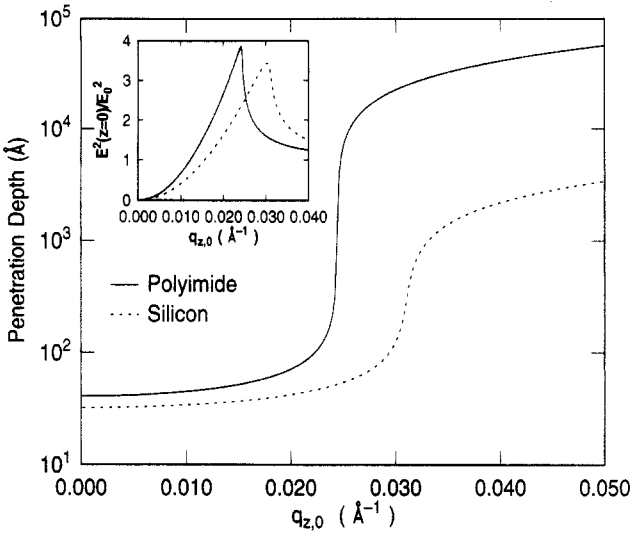

Figure 2. Penetration depth as a function of the q_z for polyimide. The penetration depth increases sharply at $q_{z,c}$ which is 0.024 Å^{-1} for polyimide and 0.031 Å^{-1} for silicon. The inset shows the electric field intensity at the surface divided by the incident intensity, $E^2(z = 0)/E_0^2$.

the wafer and then at 2500 rpm for 30 s. The sample was then heated on a hot plate at 80–85 °C for ~10 min to remove most of the solvent. This produced films with uniform thickness, as judged by the homogeneity of the interference color. The molecular weights of the polymers were $\sim 2.3 \times 10^3$ with a weight to number average molecular weight ratio of 2.

All samples were annealed under flowing nitrogen. Different heating profiles were employed for each annealing temperature and are listed below.

·100 °C. The specimen was placed on a hot plate at 100 °C for 2 h.

·250 °C. The specimen was heated at 3 °C/min to 150 °C and then at 5 °C/min to 250 °C and held at 250 °C for 90 min.

·300 °C. The specimen was heated at 3 °C/min to 150 °C and then at 5 °C/min to 300 °C and held at 300 °C for 60 min.

·420 °C. The specimen was heated at 3 °C/min to 150 °C, at 5 °C/min to 300 °C, and then at 8 °C/min to 420 °C and held at 420 °C for 30 min.

After annealing, the specimens were cooled at a rate of 10–15 °C/min. Film thicknesses were then measured by ellipsometry and X-ray reflectivity. Further reference to the sample preparation, film thickness, and precursor will be abbreviated. For example, 2500 Å/300 °C refers to a 2500-Å-thick polyimide film heated to 300 °C.

GIXS measurements were performed on a beamline X20C at the National Synchrotron Light Source (NSLS).[21] A torroidal mirror was used to focus the beam at the specimen position and effectively cut off radiation above ~10.5 keV. The incident beam had a vertical divergence of ~0.2 mrad, and the horizontal divergence was limited to about 1 mrad by a slit close to the source (S1 in Figure 1). The scattering measurements were performed using a four circle spectrometer with the sample nearly vertical. The monochromator was a pair of synthetic multilayers composed of alternating layers of Si and W with a repeat distance of either 22.3 or 23.5 Å and had an energy band-pass ($\Delta\lambda/\lambda$) of 1.1–1.2%.[21] Given the low scattering power of polymers and the small scattering volume, the multilayer monochromator was essential to the success of these experiments. X-ray energies of 6.25, 6.99, and 7.96 keV were used in these studies and the incident flux onto the sample was $\sim 2 \times 10^{11}$ photons/s at 200 mA of storage ring current.

A schematic diagram of the experimental setup is shown in Figure 1. A 75–200-μm slit (S3) was used to define the horizontal width of the incident beam and confined the beam to the specimen surface at small angles of incidence. Slits with a 2-mm separation defined the vertical size of the incident beam. These slits were followed by a 25-μm Kapton film oriented at 45° with respect to the incident beam. The scattering from this film ($\sim 2 \times 10^4$ counts/s at 150 mA) served as a monitor for the incident flux. Soller slits of 1- or 2-mrad acceptance were used to define the direction of the scattered beam. The height of the slits at the detector (S5) was set so that the area on the specimen viewed by the detector did not exceed the area illuminated by the incident beam. The angular acceptance out of the scattering plane was between 4 and 10 mrad. A set of slits (S4) between the sample and the Soller slits was used to eliminate stray radiation. The combination of the mirror, monochromator, and energy discrimination minimized contributions from harmonics. During measurements, the sample was blanketed in a helium atmosphere to reduce air scattering and to minimize sample degradation in the high flux of the incident beam. To ensure that degradation had not occurred, the samples were translated in the beam to expose a fresh portion of the samples and selected experiments were repeated. Excellent reproducibility was found. Surface sensitive scans required approximately 2 h to complete, whereas those with bulk sensitivity took approximately 30 min.

Grazing Incidence X-ray Diffraction. For X-rays, the index of refraction of a material is slightly less than unity and is given by[22-24]

$$n = 1 - \delta - i\beta \tag{1}$$

where

$$\delta = N_A \rho_{el} \lambda^2 r_0 / 2\pi \tag{2}$$

and

$$\beta = \lambda\mu / 4\pi \tag{3}$$

N_A is Avogadro's number, ρ_{el} is the molar electron density, r_0 is the classical electron radius (2.82×10^{-13} cm), μ is the linear attenuation coefficient, and λ is the X-ray wavelength. The angle for total external reflection of X-rays with respect the vacuum, commonly termed the *critical angle*, is given by

$$\alpha_c = \sqrt{2\delta} \tag{4}$$

For incidence angles less than α_c nearly all of the radiation is totally reflected. For convenience we refer to q_z, the component of the scattering vector normal to the surface, rather than the angle of incidence. With this, the critical q_z is

$$q_{z,c} = (4\pi/\lambda)\alpha_c = 2\sqrt{N_A \rho_{el} r_0} \tag{5}$$

The crux of the GIXS technique is that the penetration depth of the X-rays can be varied by changing q_z. The penetration depth $\Lambda(q_z)$ characterizing the exponential decay[25] of the intensity is shown in Figure 2. For $q \leq q_{z,c}$, surface sensitivity (~50 Å) is achieved. Interference between the air/polymer and polymer/substrate interfaces results in an electric field intensity which is not an exponential decay. The effects of multiple reflections from the substrate were incorporated in the analysis and are described in Appendix A.

Scattering measurements were performed using a symmetric four circle diffraction geometry where the angles of the incident

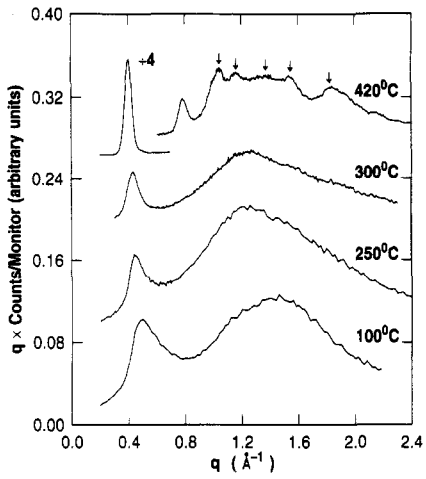

Figure 3. Bulk sensitive diffraction from PMDA–ODA films cured from *p*-PAE. With increasing annealing temperature, the first peak shifts to a smaller scattering vector and narrows, implying that the order parallel to the chain axis increases with annealing temperature. For the 420 °C film, the first reflection has become considerably more intense and new reflections have appeared (see arrows). These are indicative of increased order parallel and perpendicular to the chain axis, respectively. In this figure, as well as those to follow, the baseline in the intensity is floated to make the presentation easier to follow.

and diffracted beams with respect to the substrate surface, α and β, are equal[26,27] (see Figure 1). The scattering vector $\vec{q}$ is characterized by the components q_x and q_z which are parallel and perpendicular to the surface, respectively. Measurements were performed as a function of the scattering vector $q[=(4\pi/\lambda)\sin\theta]$ at constant values of q_z. By measuring the intensity at different q_z above and below $q_{z,c}$, the structure of a material near the surface can be distinguished from that of the bulk. Since the horizontal acceptance of the detected beam was much larger than the horizontal divergence of the incident beam, the incident beam determined the penetration depth of the X-rays.

Results

A. Bulk Structure of *p*-PAE. Figure 3 shows the diffraction profiles from films of *p*-PAE that were at least 2500 Å in thickness and were annealed at 100, 250, 300, and 420 °C. The data were obtained using GIXS for $q_z > q_{z,c}$ where the incident X-rays penetrate into the bulk of the sample. The films were found to be isotropic about the surface normal, but the polymers are oriented parallel to the surface which is consistent with previous results.[28,29] As can be seen, the first peak shifts to a smaller scattering vector with increasing annealing temperature. For the uncured specimen, the first peak is centered at 0.48 Å^{-1}, while for the specimen cured at 420 °C, it has shifted to 0.40 Å^{-1}. Furthermore, this reflection intensifies and narrows with increasing annealing temperature. For the 100, 300, and 420 °C specimens the full widths at half maximum (FWHM) are 0.17, 0.09, and 0.056 Å^{-1}, respectively. Finally, the 100 °C specimen contains a broad halo centered at 1.5 Å^{-1}, while for the 250 and 300 °C specimens, this is centered at 1.3 Å^{-1}. The 420 °C specimen has several new reflections characteristic of a more ordered system.

The reflections at low q in Figure 3 are due to order along to the chain axis. Referring to the structure above, the *d*-spacing corresponding to this reflection is the average projected length of the monomer unit onto the chain axis. Larger *d*-spacings correspond to a more planar zigzag conformation of the molecule.[30] The monomer length is 18 Å, and a planar zigzag conformation yields a *d*-spacing of 16.2 Å.[30] For the 100 °C specimen this projected length is about 13 Å, whereas for the specimens cured at 250, 300, and 420 °C, the *d*-spacings are 14, 14.6, and 15.6 Å, respectively. Thus with increasing annealing temperature the polymer adopts a more planar zigzag conformation.

Even at the highest annealing temperatures, the polyimide has not achieved the highest degree of ordering possible, since the *d*-spacing of the low reflection is less than that for a planar zigzag conformation. This is also manifested in the breadth of this reflection which results from imperfections in the ordering (e.g., finite crystal size, inhomogeneous crystal strain and lattice distortions[27,31–35]) and is described by a coherence length. This is the average distance over which the diffraction planes persist, and we define the coherence length as $2\pi/\Delta q$, where Δq is the FWHM of the reflection. For the data shown in Figure 3, the coherence length increases from 60 to 120 Å with increasing annealing from 100 to 400 °C. For comparison the persistence length measured by low angle light scattering for the precursor *p*-PAE in solution (which reflects the rigidity of the parent molecule) is 45 Å.[36] Thus, for the 100 °C annealed film, the local extension of the molecule is quite low, only one and one half times that seen in solution. As the annealing temperature is increased, the local extension of the polymer increased, but not dramatically.

The appearance of reflections at higher q for the 420 °C specimen demonstrates that ordering is enhanced for this highest annealing temperature. In fact, it approaches a crystalline ordering, and for this reason, we describe this structural order as "crystalline-like". This also distinguishes this order from the "liquid crystalline-like" order in the polyimides annealed at lower temperatures. Fiber diagrams of Kazaryan et al.[30] show that for the crystalline-like state the unit cell is orthorhombic (a = 6.31 Å, b = 3.97 Å, and c = 32 Å) with the planar zigzag polyimide chain along the *c*-axis. Using this unit cell, the reflections at 0.40 and 0.78 Å^{-1} are consistent with the (002) and (004) reflections. The peak at 1.0 Å^{-1} corresponds to an overlap of the (102) and (101) reflections whereas the reflections at 1.15 and 1.52 Å^{-1} can be attributed to the (103) and (010) lattice planes. The non (00l) reflections lie in directions which are not parallel to the chain axis and, therefore, imply the existence of order perpendicular to the chain axis. The diffraction profiles for specimens annealed at low temperatures only exhibit halos centered at 1.5 or 1.3 Å^{-1}. This implies short range correlations between neighboring chains. The shift from 1.5 Å^{-1} for the 100 °C specimen to 1.3 Å^{-1} for the higher temperature anneals reflects a denser lateral packing of the chains upon annealing.

In keeping with the results of Takahashi et al.,[29] the data for *p*-PAE indicate that the polyimide chains become locally more extended with increasing annealing temperature (i.e., the *d*-spacing of the (002) reflection increases). This is consistent with the observed increase in the coherence length for this reflection. With the appearance of new non (00l) reflections for the 420 °C specimen, the order perpendicular to the chain must also increase. The transition to a more highly ordered state for temperatures in excess of 375 °C agrees with the diffraction data of Takahashi et al.[29] and the bulk density measurements of Russell,[37] where a sharp increase in the density was found at 375 °C.

B. GIXS on *p*-PAE. B.1. Thick Films. The results for the thickest films, between 2500 and 3300 Å, are presented in a manner which emphasizes the differences between the surface and bulk structure. Scans where $q_z > 0.022$ Å^{-1} ($\Lambda \gtrsim 100$ Å) are referred to as bulk sensitive, while scans where $q_z < 0.022$ Å^{-1} ($\Lambda \lesssim 100$ Å) are termed surface sensitive. Recall that $q_{z,c} = 0.024$ Å^{-1}.

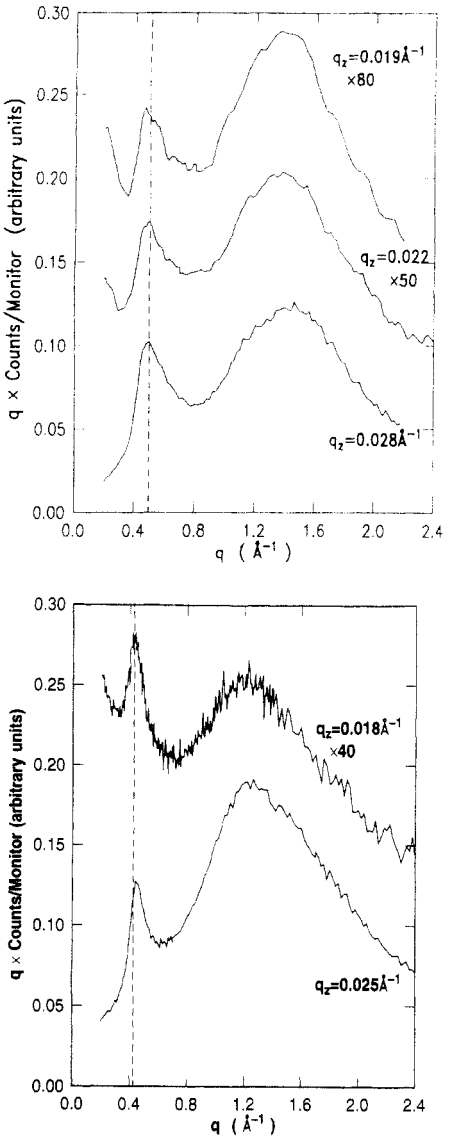

Figure 4. (a, top) Diffraction profiles for several q_z for 3300 Å/100 °C. With increasing surface sensitivity, the first reflection shifts to a smaller q and narrows. (b, bottom) Diffraction profiles for 3300 Å/250 °C at q_z = 0.025 Å^{-1} and q_z = 0.018 Å^{-1}, which represent bulk and surface sensitive diffraction, respectively. For surface sensitivity, the first reflection is centered at a smaller q and is narrower than that for bulk sensitivity. This indicates that the chains are slightly more extended at the surface. The vertical lines are drawn for reference.

Diffraction profiles for the 3300 Å/100 °C specimen are shown in Figure 4a. At this temperature there has been only minimal conversion of the amic acid ester to the corresponding imide. Between bulk and surface sensitivity, the first reflection shifts from 0.495 to ~0.475 Å^{-1}, as determined from a Lorentzian fit (see Appendix C). This corresponds to an increase in the d-spacing from 12.7 to 13.2 Å. Also, the FWHM of the first reflection decreases from 0.18 to 0.11 Å^{-1}, corresponding to an increase in the coherence length from 35 to 55 Å. These observations are consistent with a liquid crystalline-like order throughout the film, but in the vicinity of the surface the p-PAE chains are locally more extended in the direction parallel to the surface. [Since many of our results are based on the accurate measurement of reflection positions, it is important to consider how the technique itself alters the measured reflection positions. The effects of refraction on the magnitude of q_z are not important, and systematic errors in the estimated area correction factor are unlikely to cause the reflection to shift slightly. Nonetheless, the most convincing argument that the peak shift is not an artifact of the measurement is that GIXS on another polymer, poly(hexyl–pentylsilane), does not show a shift of the observed reflections, nor appreciable changes in width.[19]]

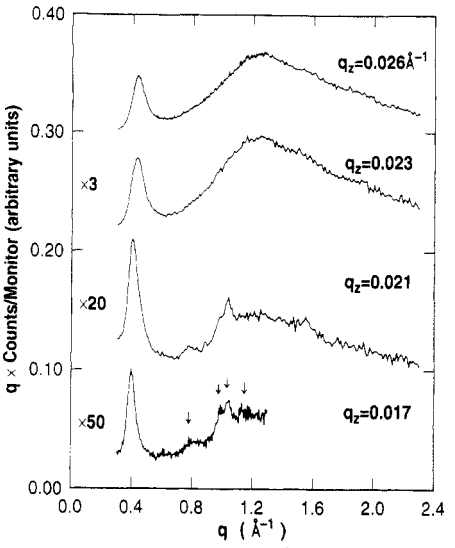

Figure 5. Diffraction from 2500 Å/300 °C at different q_z. Between bulk and surface sensitive q_z, dramatic changes in the diffraction occur. For $q_z \leq 0.021$ Å^{-1}, higher order reflections appear to 0.79, 0.99, 1.04, and 1.15 Å^{-1}, as indicated by the arrows. Furthermore, the first reflection shifts to a smaller q and becomes sharper. The surface sensitive diffraction is consistent with a crystalline-like ordering of the polyimide. In contrast, the bulk is in a liquid crystalline-like state.

The diffraction profiles for 3300 Å/250 °C in Figure 4b contain a reflection near 0.43 Å^{-1} and a diffuse halo centered at 1.3 Å^{-1}. Between bulk and surface sensitive q_z, the first reflection shifts from 0.452 to 0.426 Å^{-1}, as determined from a Lorentzian fit (see Appendix C). This corresponds to an increase in the d-spacing from 13.9 to 14.7 Å, which demonstrates that the polyimide chains are more extended at the surface than in the bulk. The FWHM of this reflection stays constant at a value of approximately 0.12 Å^{-1}, which corresponds to a coherence length of 50–60 Å. This invariance shows that the extension of the chain at the surface occurs *only locally* and that, on average, the ordered regions at the surface are not significantly larger than those found in the bulk.

The diffraction profiles for 2500 Å/300 °C are shown in Figure 5 and exhibit dramatic changes between surface and bulk measurements. In the bulk measurement a reflection is observed at 0.434 Å^{-1} and has a FWHM of 0.09 Å^{-1}. This corresponds to a Bragg spacing of 14.5 Å with a coherence length of ~70 Å. Near the surface, however, the reflection has shifted to 0.397 Å^{-1} and the FWHM is only 0.06 Å^{-1}, which corresponds to a Bragg spacing of 15.82 Å and a coherence length of 100–120 Å. Furthermore, *higher order reflections* appear at 0.79, 0.99, and 1.04 Å^{-1}, which can be indexed as (004), (101), and (102) reflections. The ratio of the (004) to the (002) integrated intensities is 0.08–0.10, while that for the (101) and (102) reflection is 0.2–0.3. The bulk diffraction profiles show that the interior of the sample is in a liquid crystalline-like state. In contrast, in the surface sensitive case, the diffraction profile resembles that observed for polyimide in the crystalline-like state (see Figure 3).

The reflection near 0.4 Å^{-1} can be decomposed into the sum of two reflections. These were modeled as a Lorentzian peak centered at 0.434 Å^{-1} and a Lorentzian raised to the 6.7 power (denoted L6.7) centered at 0.397 Å^{-1}, and

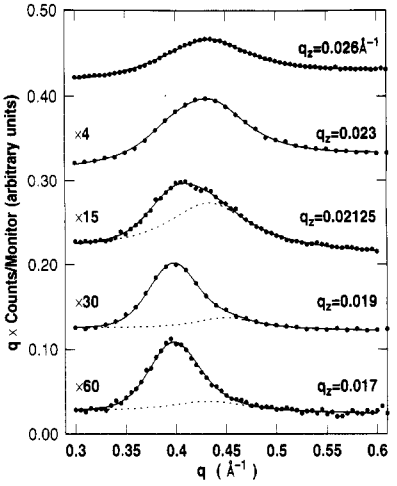

Figure 6. Calculated fits to the first peak of 2500 Å/300 °C for different q_z. These fits are a superposition of bulk and surface contributions centered at 0.397 and 0.434 Å^{-1}, respectively. The dotted line represents the bulk contribution.

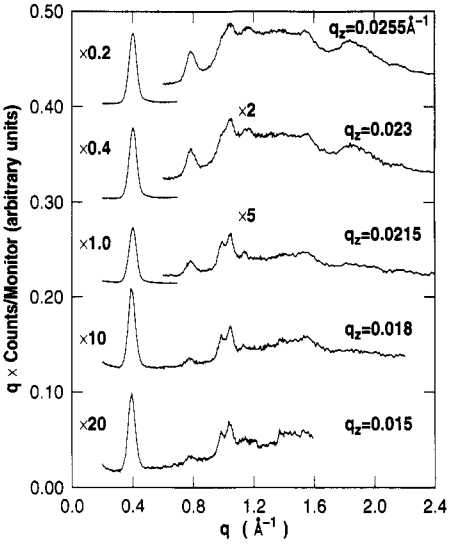

Figure 7. Diffraction profiles of 2500 Å/420 °C for several q_z. For $q_z < 0.022$ Å^{-1}, distinct peaks appear which are consistent with the (101) and (102) reflections and are indicative of enhanced ordering perpendicular to the chain axis. For clarity, the data in the top three traces have been multiplied by separate scale factors at small and large q.

they are identified as the surface and bulk contributions, respectively. Since the 0.397- and 0.434-Å^{-1} peaks overlap, care was exercised in fitting the peaks. When the peaks were of comparable intensity, the position and width of both were fixed; otherwise the more intense reflection was fitted while the parameters for the other were held fixed. Examples of the fits are shown in Figure 6. The results of the fits will be described below.

The data from selected scans of the 2500 Å/420 °C sample are shown in Figure 7 for several q_z. The most striking feature in these data is the appearance of two distinct reflections when the scattering becomes surface sensitive. These are seen at 0.987 Å^{-1} (the (101) reflection) and 1.044 Å^{-1} (the (102) reflection), and their positions do not change as q_z decreases. The line shapes of these peaks together with the (004) reflection are shown in Figure 8 to emphasize the enhancement of the (101) and (102) peaks.

The data in Figure 7 show that the position of the (002) peak decreases as q_z becomes surface sensitive, and Figure 9 shows the d-spacings calculated from the (002) and (004) reflections. [The ratio of the (004) peak position to that of the (002) is less than 2 (i.e., ~1.95). This results from

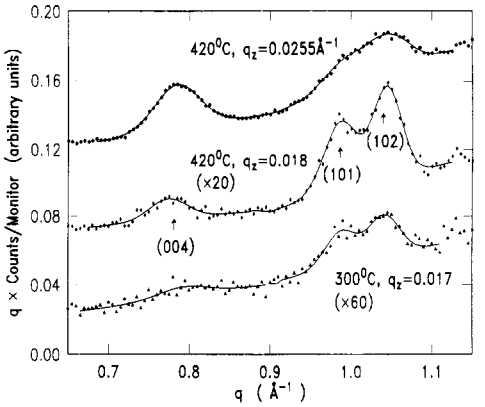

Figure 8. Calculated fits to the (004), (101), and (102) reflections of 2500 Å/300 °C and 2500 Å/420 °C. Between the surface and bulk sensitive scans for 2500 Å/420 °C, the FWHM of the (101) and (102) reflections increases from ~0.04 to ~0.06 Å^{-1}. Thus in the direction perpendicular to the chain axis, the coherence length is ~50% larger at the surface than in the bulk. For the surface sensitive scan of 2500 Å/300 °C, the FWHM of the (101) and (102) reflections is ~0.05 Å^{-1}.

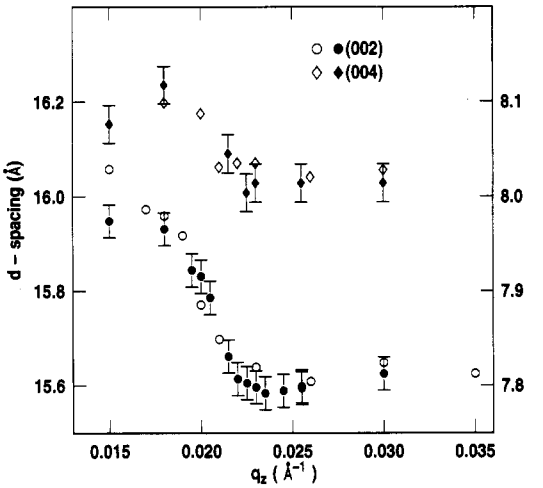

Figure 9. d-spacings for the (002) and (004) reflections as function of q_z for 2500 Å/420 °C. For the (002) reflection, the d-spacing increases by about 0.35 Å. The (004) d-spacing, by contrast, increases less than 0.1 Å. The halfway point in the shift is at $q_z = 0.020$ Å^{-1}, which corresponds to an incident X-ray penetration depth of about 70 Å. The error bars (±0.08 Å) correspond to the error in the fitting procedure. Open and filled circles represent data obtained during different experimental runs. Error bars are shown only for the filled symbols for clarity.

a negatively skewed distribution of the projection of the 18-Å monomer unit length onto the chain axis[32,40-42] (see Appendix C).] Between bulk and surface sensitivity, the d-spacing for the (002) reflection increases from 15.6 to 15.95 Å. This increased spacing suggests that the projection of the monomer unit onto the chain axis increases in the vicinity of the free surfae and indicates that the polymer chain adopts a more planar conformation near the air interface. The d-spacing that is halfway between the bulk and surface values is found for $q_z \sim 0.02$ Å^{-1}, which corresponds to an X-ray penetration depth of ~70 Å. This provides a rough estimate for the depth to which the surface effects persist. The d-spacings for the (004) reflection are 8.02 Å in the bulk and 8.09 Å at the surface, and therefore, the shift is much smaller for this reflection than for (002). The ratio of the (002) and (004) d-spacings changes from 1.955 in bulk to 1.975 at the surface. In terms of the paracrystalline model (see Appendix C), this is consistent with improved order parallel to the chain axis near the air surface.

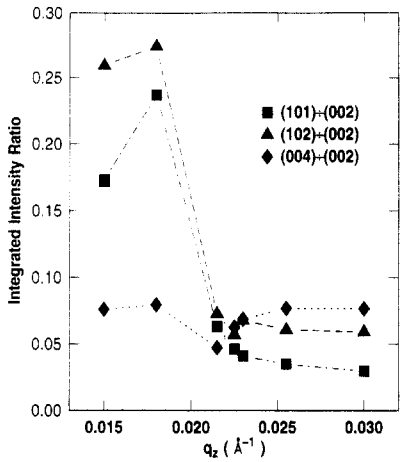

Figure 10. Ratios of the (004), (101), and (102) integrated intensities to that of the (002) reflection for 2500 Å/420 °C. The ratio of (004) to (002) is ~0.08 at both surface and bulk sensitive q_z, while the ratio of (101) and (102) to (002) is much larger at surface sensitive values of q_z. These data show that near the surface the order normal to the chain axis is increased more than order parallel to the chain axis.

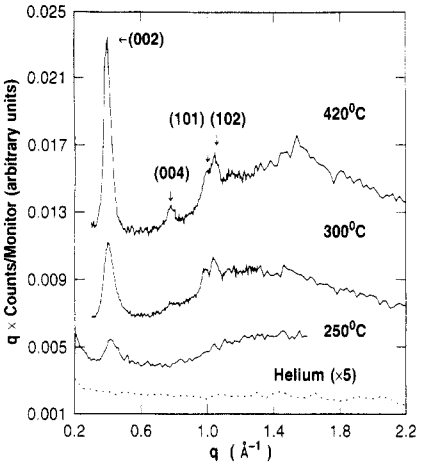

Figure 11. Diffraction for 100-Å thin films cured from *p*-PAE. The films cured at 420 and 300 °C appear to be in the crystalline-like state, while the film cured at 250 °C is liquid crystalline-like. For each film, the structure throughout the film was sampled, as q_z was above the critical value for polyimide. The monitor rate for the 100 Å/250 °C specimen was approximately twice that for the other profiles. The helium background is shown for the purpose of comparison.

Coherence lengths were estimated from the widths of the (002) and (004) reflections after correction for the instrumental resolution. For the (002) reflection, the coherence length is ~115 Å, whereas for the (004) reflection, this is ~110 Å. For the bulk and surface sensitive data, the coherence lengths for these reflections are the same, to within errors. This strongly suggests that (1) the extent of ordering along the chain axis is the same in the bulk as near the air surface and (2) the perturbations to the molecular conformations due to the surface are only local.

For the (101) and (102) reflections, however, dramatic changes are seen between the bulk and surface sensitivity measurements. The fitted widths for both peaks were ~0.04 Å^{-1} at the surface and ~0.06 Å^{-1} in the bulk. After quadrature subtraction of the instrumental resolution, the calculated coherence lengths for both reflections increased from ~120 Å in the bulk to ~170 Å at the surface. Thus, the coherence length is larger *perpendicular* to the chain axis rather than *parallel* to it. By contrast, for bulk polyimides that have been annealed at lower temperatures, there is much less order perpendicular to the chain axis.

The ratios of the (004), (101), and (102) integrated intensities to that of (002) are shown in Figure 10 and provide insight into the surface ordering. The ratio of the (004) and (002) intensities remains constant at 0.08, while intensities of (101) and (102) increase with respect to both (002) and (004). This provides further evidence that the presence of a free surface enhances the ordering perpendicular to the chain axis more than the ordering parallel to the chain axis.

In summary, for 2500 Å/420 °C, several differences between the bulk and surface diffraction are noted. The surface sensitive diffraction shows larger *d*-spacings for the (002) and (004) reflections as well as narrower and more intense (101) and (102) reflections as compared with the bulk. These results show that the polyimide chains within about 70 Å of the surface are contained in domains that are more ordered along the chain axis. Perpendicular to the chain axis, the domains are significantly larger and more ordered at the surface than in the bulk.

B.2. Thin Films. *p*-PAE films ~100 Å in thickness were prepared with annealing treatments identical to those of their thick film counterparts. The GIXS measurements were taken at q_z slightly below the critical q_z for the silicon substrate and, therefore, the structure throughout the film was sampled. The diffraction profiles are shown in Figure 11.

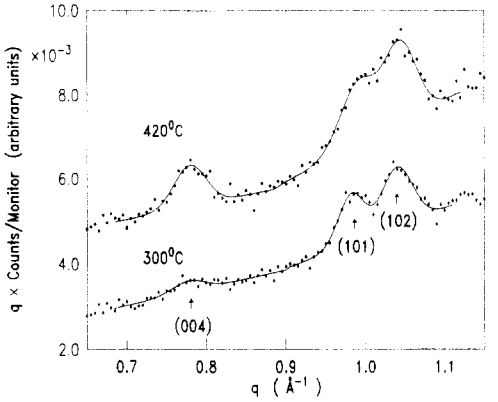

Figure 12. Calculated fits to the (101) and (102) reflections of 100 Å/300 °C and 100 Å/420 °C. The reflections are more distinct for the 300 °C film than for the 420 °C film. The fitted FWHM's for the both (101) and (102) are ~0.04 and ~0.05 Å^{-1} for the 300 and 420 °C films, respectively.

As for the thicker films, the amount of order increases with annealing temperature. The 100 Å/250 °C film shows a peak at 0.42 Å^{-1} with a width of 0.08 Å^{-1}, and there is a diffuse halo centered near 1.4 Å^{-1}. This profile is consistent with a liquid crystalline-like ordering and is comparable to the profile for the bulk of 2500 Å/300 °C, except that the 100-Å film has a narrower first peak centered at smaller q.

The diffraction from 100 Å/300 °C is significantly different from that of 100 Å/250 °C but is comparable to that observed for 2500 Å/300 °C near the surface. The (002) reflection is centered to 0.399 Å^{-1} and has a width of 0.056 Å^{-1}. The (004) reflection also appears, albeit weakly. In addition, the (101) and (102) reflections are distinctly present as shown in Figures 11 and 12 and have FWHM's of ~0.04 Å^{-1}. This shows that the order perpendicular to the chain axes extends over a larger distance than that parallel to the chain axis. Therefore, 100 Å/300 °C is in a *crystalline-like* state.

For 100 Å/420 °C the (002) reflection is centered at 0.396 Å^{-1} with a width of 0.049 Å^{-1}. The (004) reflection appears at 0.786 Å^{-1}, and the (101) and (102) reflections

are also present (see Figures 11 and 12). Thus, the 100 Å/420 °C film is crystalline-like. However, while the order parallel to the chain axis is better in this film than in 100 Å/300 °C and the surface of 2500 Å/420 °C, the opposite is true for order perpendicular to the chain axis. This is evidenced as follows: (i) For 100 Å/420 °C, the (101) and (102) peaks (FWHM's ~0.05 Å^{-1}) are not as distinct as for 100 Å/300 °C or the surface sensitive data for 2500 Å/420 °C. (ii) Further support is found by examining the ratio of the integrated intensities of the extended and less-extended components of the (002) reflection (centered at 0.396 and 0.434 Å^{-1}, respectively). For 100 Å/420 °C this ratio is about 6, much larger than for 100 Å/300 °C (with a ratio of 1.7). We believe that the difference in the parallel and perpendicular order may be due to strong interactions between the polyimide and the Si substrate at elevated temperatures.

Experiments were also performed at several surface sensitive q_z, and no change in the peak shape and position of the (002) reflection was found. This result suggests that thin films are uniform in structure throughout the film.

B.3. Films of Intermediate Thickness. Two films with intermediate thickness, 400 Å/300 °C and 470 Å/420 °C, were measured and analyzed as described above. The purposes of these studies were 2-fold. First, for thin films it appears that the surface induced order propagates through the entire film whereas for the thick specimens the surface induced order is limited to the top ~70 Å. This raises the question at what thickness is the bulk structure first observed. Second, the structure of the polymer at the substrate interface can be studied. Such information cannot be obtained from the thicker specimens where the scattering from the substrate interface comprises only a small fraction of the total scattering. For films ~400 Å in thickness, however, if ordering occurs at the substrate interface, then the scattering from the structure near the air and substrate interfaces will comprise a significant fraction of the total scattering.

The diffraction profiles for 400 Å/300 °C at different q_z are similar to those for 2500 Å/300 °C and are shown in Figure 13a. As q_z decreases below 0.022 Å^{-1}, the first peak narrows and shifts to smaller q and the (101) and (102) reflections appear. Under the most surface sensitive conditions, the ratio of the integrated intensities of the 0.397 Å^{-1} (surface) and 0.434 Å^{-1} (bulk) reflections is 1.5, which is smaller than that for 2500 Å/300 °C (3.5) and 100 Å/300 °C.[10] This implies that the surface of 400 Å/300 °C is less ordered than for these other films.

The diffraction profiles for 470 Å/420 °C are shown in Figure 13b and exhibit the same qualitative behavior as 2500 Å/420 °C. Likewise, the ratios of the (004), (101), and (102) integrated intensities to that of the (002) reflection are similar to that observed for 2500 Å/420 °C. The (004) to (002) intensity ratio remains constant at nearly 0.08 for all q_z. The (101) and (102) reflections increase in intensity in comparison to the (002) reflection, although not as much as for 2500 Å/420 °C. This indicates improved order perpendicular to the chain axis near the surface. Finally, the FWHM's of the (101) and (102) peaks decrease from approximately 0.06 Å^{-1} in the bulk to 0.044 Å^{-1} at the surface, corresponding to an increase in the coherence from ~110 to ~160 Å. This latter value is slightly smaller than that for 2500 Å/420 °C. Along with the smaller value of the intensity ratios, this suggests that the order perpendicular to the chain axis for 470 Å/420 °C is less than that for 2500 Å/420 °C.

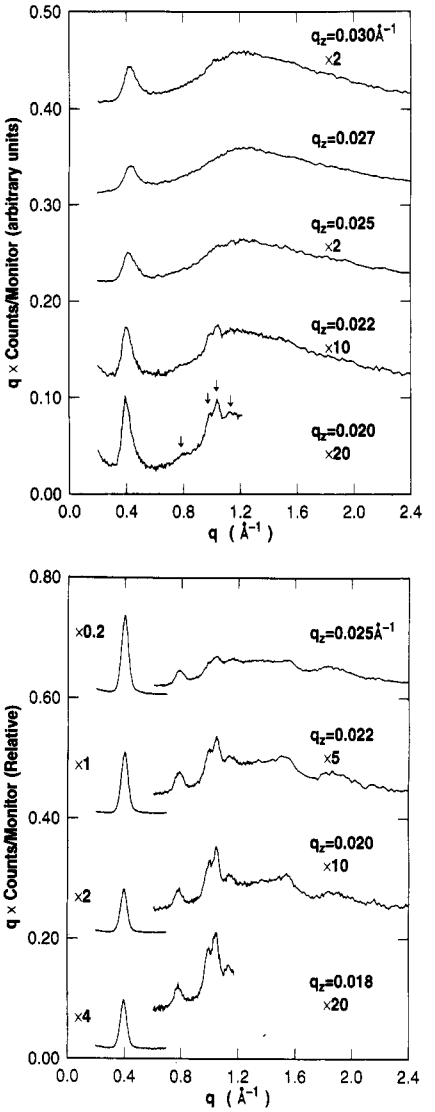

Figure 13. (a, top) Diffraction from 400 Å/300 °C at different q_z. Between bulk and surface sensitive q_z, dramatic changes occur in the diffraction. *For* $q_z \leq 0.022$ Å^{-1}, higher order reflections appear at 0.79, 0.99, 1.04, and 1.15 Å^{-1}, as indicated by the arrows. Furthermore, the first reflection shifts to a smaller q and becomes sharper. The surface sensitive diffraction is consistent with a crystalline-like ordering of the polyimide. By contrast, the bulk is in a liquid crystalline state. (b, bottom) Diffraction from 470 Å/420 °C at different q_z.

In summary, the 470 Å/420 °C specimen appears to have about the same structure as 2500 Å/420 °C. From the surface sensitive measurements the polymer ordering is markedly enhanced within ~80 Å of the air/polymer interface. What is not known is whether there is a similar enhancement of the ordering near the polymer/silicon interface. Since the bulk of 470 Å/420 °C has the same diffraction profile as 2500 Å/420 °C, the thickness of the interface region must be limited or the (101) and (102) reflections would be readily apparent in the bulk sensitive diffraction profiles. Furthermore, it was observed that the (101) and (102) reflections are sharper for the surface of 470 Å/420 °C than for 100 Å/420 °C. This shows that the ordering for 100 Å/420 °C is not as extensive and suggests that the Si/SiO_2 interface could inhibit the ordering of the nearby polymers as compared to the influence of the air surface.

Dependence of Intensity on q_z

Let $I_j(\vec{q})$ be the measured intensity for structural component j. The structure factor is $S_j(\vec{q})$ and the

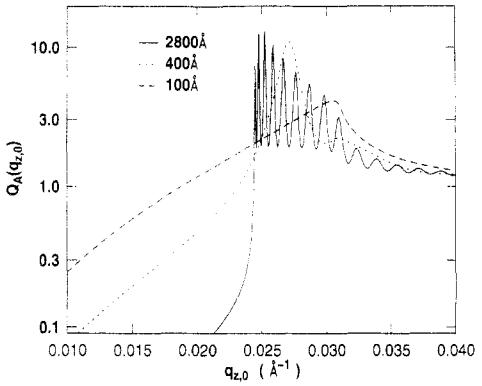

Figure 14. Models for the $Q_A(q_z)$ intensity as a function of q_z for film thicknesses of 100, 400, and 2800 Å.

concentration of diffracting material is $c_j(z)$. For the polyimide films, there are two components which are denoted A and B and correspond to the crystalline-like and liquid crystalline-like phases, respectively. The sum of the concentration of these two components is assumed to equal unity,

$$c_A(z) + c_B(z) = 1 \tag{6}$$

and only one concentration need be specified.

For a thin film on a substrate, the scattered intensity depends on the electric field in the film. An expression for the electric field, $E(k_z^{in},z)$, is given in Appendix A. Here, k_z^{in} is the z-component of the incident radiation $k_z^{in} = q_z/2$ and z is the distance from the air surface. In this model, the electric field effects for the outgoing wave are neglected. To calculate the observed intensity, the ideal intensity is convoluted by the function $R_1(q_z)$ which represents the divergence of the incoming beam perpendicular to the specimen surface. The observed intensity is then proportional to[19] ($q_z \ll q_x$)

$$I_j(q_x,q_z) \propto S_j(q_x,0)T\int dq_z\, R_1(k_z - k_z^{in})Q_j(k_z) \tag{7}$$

where

$$Q_j(k_z) = \frac{1}{T}\int_0^T c_j(z)|E(q_z^{in},z)|^2\, dz \tag{8}$$

Here, T is the film thickness and in this model, denoted the *two-interface model*, the polyimide density is assumed independent of z.

For the case of a uniform structure ($c_A(z) = 1$), calculated values of $Q_A(q_z)$ are shown in Figure 14 for several different film thicknesses. For $T = 2800$ Å, $Q_A(q_z)$ has many distinct maxima when $q_z > q_{z,1}$, the critical q_z of polyimide. For the thinner films, the intensity of the maximum in $Q_A(q_z)$ increases with increasing thickness, while the position of the maximum in q_z decreases. Note that one should not misinterpret this as an increase in the critical angle due to a change in film density. When only a single thick polymer layer exists, or the polymer and substrate have the same index of refraction, a simpler model can be obtained. In this case, the electric field intensity decays exponentially as a function of z. We note that this model failed to describe accurately the integrated intensity data and, therefore, was not used.[19]

The two-interface model for the intensity of the (002) reflection can be compared for 2500 Å/420 °C, 470 Å/420 °C, and 100 Å/420 °C. The concentration of the crystalline-like phase is assumed to be 100%, while that for the liquid crystalline-like phase is zero, i.e.

$$c_A(z) = 1 \quad \text{and} \quad c_B(z) = 0 \tag{9}$$

In assuming a uniform structure for the polymer films, the analysis of the (002) intensity provides a test of how well the model works. Figure 15 shows the intensity of the (002) reflections for these films together with model calculations.

In the calculations the incident beam divergence was modeled with a Gaussian with a FWHM of 0.5 mrad. The

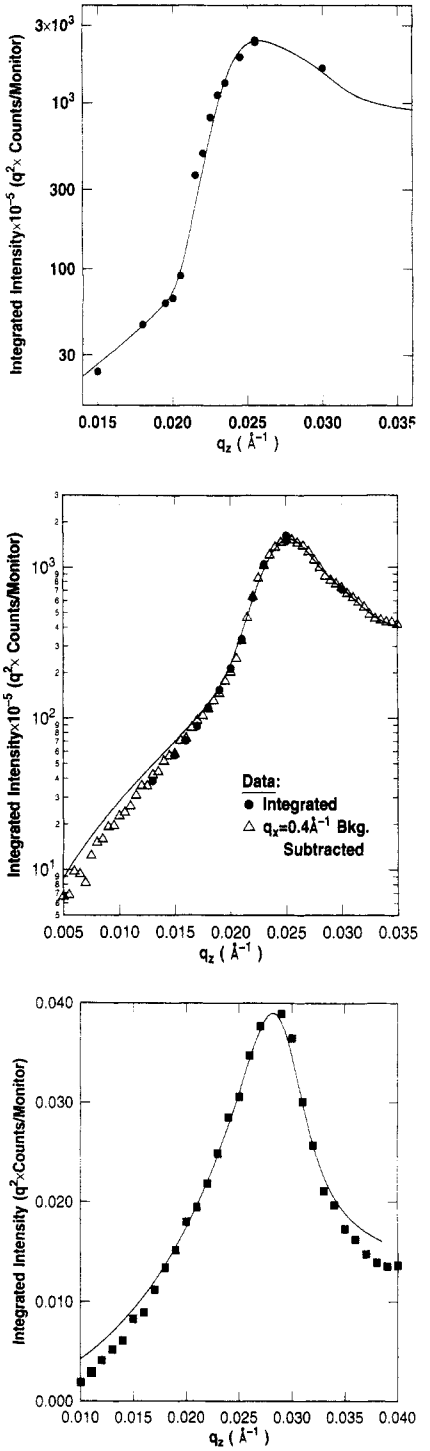

Figure 15. Comparison of the fits to the (002) intensity. (a, top) Integrated intensity for 2500 Å/420 °C. (b, middle) Integrated intensity and peak intensity at $q_x = 0.4$ Å^{-1} for 470 Å/420 °C. The latter has been scaled to match the integrated intensity at the peak in q_z. (c, bottom) Peak intensity at $q_x = 0.4$ Å^{-1} for 100 Å/420 °C. Since the reflection width varies little with q_z, the peak intensity at $q_z = 0.4$ Å^{-1} is approximately proportional to the integrated intensity.

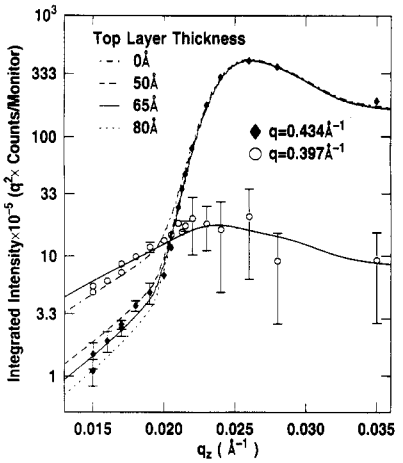

Figure 16. Integrated intensity of the 0.434-Å^{-1} reflection of 2500 Å/300 °C is compared to fits for the two-interface model. The dot-dashed line corresponds to no crystalline-like layer, the dashed line to a 50-Å layer, the solid line to a 65-Å layer, and the dotted line to an 80-Å layer. The solid line through the 0.397-Å^{-1} data assumed the 65-Å thickness and was scaled to provide the best fit.

polyimide critical q_z was 0.0244 Å^{-1}, and the model q_z values were offset to provide the best fit to the data, as determined visually. The other parameters were the film thickness, the silicon critical q_z of 0.031 Å^{-1}, and the polyimide and silicon absorption lengths of 1 and 0.07 mm, respectively. As is evident in Figure 15, the two-interface model provides a good fit to the data for all films.

Once confidence is established in the model, the thickness of the top layer can be assessed. The diffraction profiles of the first reflection of 2500 Å/300 °C at different q_z indicate that the surface is crystalline-like while the bulk is liquid crystalline-like. The integrated intensity data for the 0.397- and 0.434-Å^{-1} reflections can be used to determine the thickness of the crystalline-like layer. A model was used where the top layer consists of a crystalline phase of thickness L while the bulk is liquid crystalline, i.e.

$$c_A(z) = \begin{cases} 1 & \text{for } 0 \le z \le L \\ 0 & \text{for } L \le z \le T \end{cases} \quad (10)$$

The data for the 0.434-Å^{-1} reflection was used in the model fit, since these data have a larger dynamic range and have smaller errors than the intensities for the 0.397-Å^{-1} peak. The results for crystalline-like layer thicknesses of 0, 50, 65, and 80 Å are shown in Figure 16, and as can be seen, a thickness of 65 Å gives the best fit. In the figure, the line through the 0.397-Å^{-1} data was calculated with this thickness and scaled for the best fit.

Since less-ordered regions must exist between the crystalline-like domains, the existence of some liquid crystalline-like ordering at the surface of 2500 Å/300 °C is expected. Consequently, the integrated intensity data for 2500 Å/300 °C were compared to models with different thicknesses and concentrations of the crystalline-like layer near the air surface. These are given by

$$c_A(z) = \begin{cases} c_0 & \text{for } 0 \le z < L \\ 0 & \text{for } L \le z \le T \end{cases} \quad (11)$$

where $0 \le c_0 \le 1$ is the concentration fraction of the crystalline-like phase in the top layer.

For a given thickness of the top layer, the concentration of the liquid crystalline-like material, $1 - c_0$, was adjusted to fit the data for the 0.434-Å^{-1} reflection, and several fits are plotted in Figure 17a. For layer thicknesses of 65, 120, and 300 Å, the best fits were obtained for $1 - c_0 = 0\%$, 25%, and 33%, respectively, with an error of approximately

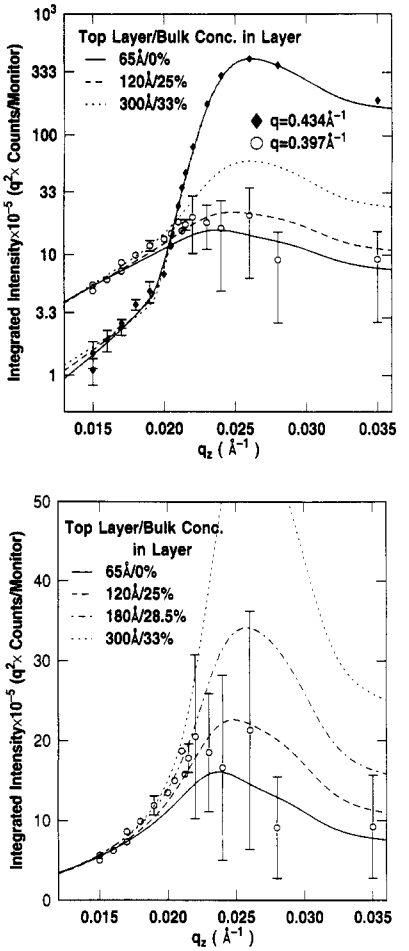

Figure 17. Models for several different concentrations of liquid crystalline material within the top layer of 2500 Å/300 °C for top layer thicknesses from 65 to 300 Å and concentrations of liquid crystalline ordering from 0 to 33%. These are compared to the data for the (a, top) 0.434-Å^{-1} and (b, bottom) 0.397-Å^{-1} reflections. The models for the 0.397-Å^{-1} reflection were scaled to match the data at small q_z. In (b), models for a 120- and 180-Å layers fit well to the surface reflection at 0.397-Å^{-1} data, while the 65-Å model appears to undershoot most of the data the 300-Å model overshoots the data. While the different layer thicknesses are not easily distinguished for the bulk reflection at 0.434 Å^{-1}, the models for the 0.397-Å^{-1} data vary greatly.

±3%. It is clear from the figure that the models fit the data equally well, except at the smallest values of q_z(<0.016 Å^{-1}), where the slope of the fits decrease as c_0 increases. While the data agree best with L = 65 Å, the differences between the fits are not significant. This shortfall in this type of modeling has been observed by other investigators.[39]

Next, the models were compared to the 0.397-Å^{-1} reflection, which arises from the crystalline-like material at the surface. In Figure 17b, the models were scaled to fit the data at the smallest q_z. The models with a 120–180-Å top layer show the best agreement with the data, while the 65-Å model undershoots the data and the 300-Å model overshoots by a large amount. Thus, in the context of this model, we estimate that the surface ordered layer is 120–180 Å thick and contains about 70% crystalline-like polyimide and 30% liquid crystalline-like polyimide. This is comparable to that for 2500 Å/420 °C, where we estimate the surface layer thickness as ≃70 Å.

Order at the Silicon Interface. Can the presence of order at the Si/SiO$_2$ surface be discerned? To examine this question, we compared the integrated intensity for 400 Å/300 °C to models where the crystalline-like order exists at the Si/SiO$_2$ interface. The concentration profile

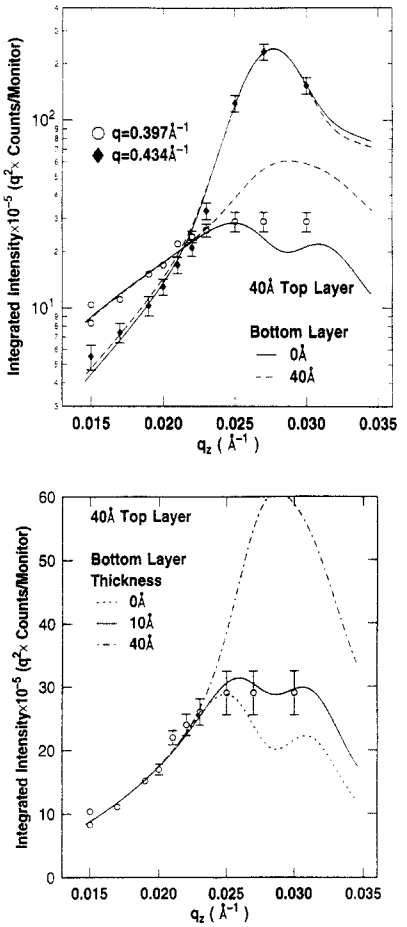

Figure 18. (a, top) Comparison of two interface models to the integrated intensities of the 0.434- and 0.397-Å^{-1} reflections in 400 Å/300 °C. The solid line corresponds to the case where a crystalline-like layer exists only at the air surface with a thickness of 40 Å. The dashed line corresponds to the case where a crystalline-like layer exists at the air and substrate interfaces with a 40-Å thickness. (b, bottom) Fits using the two-interface model to the 0.397-Å^{-1} reflection integrated intensity for 400 Å/300 °C. These are plotted for a crystalline-like layer thicknesses of 40 Å at the air surface and 0, 10, and 40 Å at the substrate surface. The 40-Å layer at the Si/SiO_2 surface does not fit the data. Models for different values of top layer thickness are not shown, but there was reasonably good agreement for values of L_1 from 30 to 50 Å. The 10-Å layer model fits the data best. This shows that the Si/SiO_2 interface enhances the polyimide ordering only slightly, or not at all.

for the crystalline-like phase is given by

$$c_A(z) = \begin{cases} 1 & \text{for } 0 \le z < L_1 \\ 0 & \text{for } L_1 \le z \le T - L_2 \\ 1 & \text{for } T - L_2 < z \le T \end{cases} \quad (12)$$

where L_1 and L_2 are the thicknesses of the layers near the air and substrate interfaces, respectively. The total thickness, T, is 400 Å, as determined by X-ray reflectivity.

Figure 18a shows the integrated intensities of the 0.434-Å^{-1} reflection (characteristic of liquid crystalline-like order) and the 0.397-Å^{-1} reflection (characteristic of crystalline-like order) together with those calculated for two different models. In the first, L_1 = 40 Å and L_2 = 0 Å, while in the second L_1 = 40 Å and L_2 = 40 Å. The first model gives a better fit to the data, although models with L_1 between 30 and 50 Å provided equally good fits. In Figure 18b, we compare the integrated intensity of the 0.397-Å^{-1} reflection with several structural models; these have different L_2, but L_1 = 40 Å. As can be seen, a crystalline-like layer thickness of L_2 = 10 Å conforms best to the data, while that with L_2 = 40 Å does not fit.

It should be noted that, in this model, 40 Å represents a minimum thickness of a crystalline-like layer at the air surface that gives an adequate fit to the data. This minimum value was chosen so as to maximize any possible order at the substrate interface. Even with this it is clear that enhanced ordering does not exist at the substrate interface. The lack of ordering at the substrate interface may result from differences in the mobilities of the polymer molecules at the air and substrate interfaces or the strong interactions of the polymer with the substrate.

Conclusions

All of the polyimide films cured from *p*-PAE precursors exhibit enhanced order near the air surface. For the films with a thickness greater than 100 Å, the order at the surface is significantly greater than that observed in the bulk. This is evidenced in several ways. First, the *d*-spacings corresponding to order along the chain axis are larger at the surface than in the bulk. This suggests that the polymer adopts a more planar zigzag conformation near the surface. This is quite reasonable since it would require only slight rotations of the chain segments about the phenyl ether linkage. The enhanced order occurs only within portions of the molecule in that no evidence was found for long range order along the chain axis (e.g., the coherence lengths were limited to ~100 Å). Second, there is an increase in the order perpendicular to the chain axis. For the films cured at 300 °C, this is demonstrated by the appearance of the (101) and (102) reflections in the surface sensitive scans. For the films cured at 420 °C, enhanced order at the surface is manifest by an increase in the intensity of the (101) and (102) peaks with respect to that of the (002) and by a narrowing of these reflections. The structure observed at the surface of the 300 °C films is qualitatively the same as that for the bulk of 420 °C films. Consequently, the transition temperature from the liquid crystalline-like to crystalline-like structure decreases from ~375 °C in the bulk to ~300 °C at the surface. In all cases, the ordering is observed only within the first ~70 Å from the free surface. In contrast to surface induced order, no enhancement of the order is observed near the substrate. Ordering at the substrate appears to be hindered. This could be the result of absorption of the polymer at the substrate, of specific interactions of the polymer with the substrate, or of the fact that an impenetrable substrate inhibits motions necessary to ordering which are possible at the penetrable air surface. Finally, it was found that 100-Å-thick films were more ordered than the corresponding thicker films subjected to the same thermal treatment.

The results of this study have several interesting implications. First, the ordering observed near the surface could dramatically alter the interdiffusion, adhesion and swelling of this polymer. The ordering observed would effectively act as a diffusion barrier for small molecule fluids and other polymers and should give rise to anomalous behavior at the onset of interdiffusion. Such behavior has, in fact, been observed in swelling studies.[43] Second, our observation of surface enhanced ordering is surprising, since such ordering is not predicted by theoretical results.[1-3] These models treat flexible amorphous polymers. Our results suggest, therefore, that the rigidity of the polymer chain and the tendency for the polymer chain to order in the bulk play an important role in surface ordering. Third, as a function of distance from the surface, the surface influence is quite rapidly damped, which is in

keeping with theoretical predictions.[1-3] Finally, the data showed a pronounced difference in the behavior of the same polymer at the air and substrate interfaces. While the former promoted order, the latter suppressed order. The exact origin of this difference needs to be understood to develop a clear picture of the influence of an interface on the conformation and intermolecular packing of polymers.

Acknowledgment. We wish to thank J. Jordan-Sweet and G. B. Stephenson for their assistance and Professor A. Bienenstock for insightful criticisms and comments on this work. T.P.R. acknowledges the support of the Department of Energy, Office of Basic Energy Sciences, Grant No. FG03-88ER45375. B.J.F. acknowledges the support of the Department of Energy, Office of Basic Energy Science, Division of Materials Sciences, through the Stanford Synchrotron Radiation Laboratory. This work was carried out (in part) at the National Synchrotron Light Source, Brookhaven National Laboratory, which is supported by the U.S. Department of Energy, Division of Materials Sciences and Division of Chemical Sciences.

Appendix A

Electric Field Effects in the Media. In this appendix, we derive an expression for the electric field in a thin film on a substrate. Since the effects of X-ray polarization are not important here, we treat the electric field as a scalar quantity. Assuming homogeneity in the x and y directions, the electric field $E(k_z^{in},0)$ is the solution of a one-dimensional wave equation[22-25]

$$\left(\frac{d^2}{dz^2} + (k_z^{in}(z))^2\right)E(k_z^{in},z) = 0 \qquad \text{(A-1)}$$

where

$$k_z(z) = \sqrt{(k_z^{in})^2 - 4\pi r_0 N_A \rho_{el}(z) - 2\pi i \mu(z)/\lambda} \qquad \text{(A-2)}$$

and where $\rho_{el}(z)$ and $\mu(z)$ are the z-dependent electron density and absorption constant defined earlier.

In a region where $\rho_{el}(z)$ and $\mu(z)$ are constant, the electric field is given by a sum of incoming and outgoing waves

$$E(k_z,t) = E^+e^{ik_z z} + E^-e^{-ik_z z} \qquad \text{(A-3)}$$

where $k_z = k_z(z)$ is a constant complex quantity. We have modeled our system as three discrete slabs where $k_z(z)$ is given by

$$k_z(z) = \begin{cases} k_z^{in} & \text{for } z \le 0 \quad \text{(vacuum)} \\ k_{z,1} & \text{for } 0 \le z \le T \quad \text{(polymer)} \\ k_{z,2} & \text{for } T \le z \quad \text{(substrate)} \end{cases} \qquad \text{(A-4)}$$

where $k_{z,1}$ and $k_{z,2}$ have been calculated using eq A-2 with the values of ρ_{el} and μ which correspond to the polymer film and Si substrate.

Within each slab, the electric field is given by eq A-3. The coefficients are determined by matching boundary conditions at $z = 0$ and $z = T$. The electric field for $0 \le z \le T$ has been calculated as[24]

$$E(k_z^{in},z) = (1 + r_1)\frac{e^{ik_{z,1}z} + r_2 e^{ik_{z,1}(2T-z)}}{1 + r_1 r_2 e^{i2k_{z,1}T}} \qquad \text{(A-5)}$$

where $r_1 = (k_z^{in} - k_{z,1})/(k_z^{in} + k_{z,1})$ and $r_2 = (k_{z,1} - k_{z,2})/(k_{z,1} + k_{z,2})$ are the reflectivities of the air/polymer and polymer/substrate interfaces, respectively.

It is also useful to know the integrated electric field intensity as a function of k_z^{in}, that is

$$I(k_z^{in}) = \frac{1}{T}\int_0^T |E(k_z^{in},z)|^2\,dz \qquad \text{(A-6)}$$

The above expression has been divided by the thickness T, to facilitate the comparison of the intensities from films of different thicknesses. The intensity is calculated as[19]

$$I(k_z^{in}) = \left[\frac{1 - e^{-\tau}}{\tau}(1 + |r_2|^2 e^{-\tau}) + 2e^{-\tau}\mathrm{Im}\left\{r_2\frac{1 - e^{i\gamma}}{\gamma}\right\}\right]\frac{|1 + r_1|^2}{|1 + r_1 r_2 e^{-\tau+i\gamma}|^2} \qquad \text{(A-7)}$$

where $\tau = 2T\mathrm{Im}\{k_{z,1}\}$, $\gamma = 2T\mathrm{Re}(k_{z,1}, 1)$ and Im and Re denote the imaginary and real parts.

In our models for the scattered X-ray intensity where a surface phase exists, the intensity is given by

$$I_\alpha(k_z^{in}) = \frac{1}{T}\int_0^T c_\alpha(z)|E(k_z^{in},z)|^2\,dz \qquad \text{(A-8)}$$

where $c_\alpha(z)$ is the concentration fraction of phase α. In our work, this has been computed numerically.

Appendix B

Profile Fitting. The positions, widths, and integrated intensities of the polyimide reflections have been determined by profile fitting. The parameters for the fitted profile as well as the values for χ^2 are tabulated elsewhere.[19] The line shapes were modeled using profiles which provided the best fit, and these were a combination of Lorentzian, Lorentzian raised to the 6.7 power (denoted L6.7), and Gaussian functions. In all of the profiles, an approximate area correction of q is multiplied by the measured intensity $I(q)$. This area correction was used rather than the more accurate correction (sin 2θ) for convenience, since the difference between these is small. The higher order reflections are rather weak, and these data were analyzed either by qualitative means or by fitting a Gaussian profile. Furthermore, since q_z was small compared to q_x, the value used for q is hardly different from q_x.

The profiles were assumed to be Lorentzian functions raised to the m power plus a linear background,

$$qI(q) = a + b(q - q_0) + \frac{1}{\pi\Delta q}\frac{2I_{int}A(m)}{\left(1 + 4\left(\frac{q - q_0}{B(m)\Delta q}\right)^2\right)^m} \qquad \text{(B-1)}$$

where $A(m)$ and $B(m)$ are multiplicative factors which maintain I_{int} as the integrated intensity and Δq is the FWHM. This function has the property of being a Lorentzian for $m = 1$ and a Gaussian for $m \to \infty$ and $B(m) = \sqrt{m}$. For $m > 20$, the function is effectively a Gaussian.

For the fits, a Marquardt nonlinear least squares fitting routine was used with an equal weighting for all of the points so as not to fit the peak at the expense of a good fit to the background. χ^2 was used to evaluate a goodness of fit, and

$$\chi^2 = \frac{1}{N - M}\sum_i\left(\frac{C_i - I(q_i)}{w_i}\right)^2 \qquad \text{(B-2)}$$

where C_i is the counts, w_i is the weighting at point q_i, N is the number of points, and M is the number of fitted parameters. The fitting algorithm was used with $w_i = 1$, while χ^2 values were computed using $w_i = \sqrt{C_i}$. Typi-

cally, χ^2 values were ~3 for fits to bulk sensitive scans, and ~1 for surface sensitive scans. This difference results because the deviations between the models and the peak shapes are greater when the count rate is larger. At low count rates, these deviations are masked by the poorer counting statistics.

Lorentzian Profile. Equation B-1 was used to fit the first reflection from the bulk of PMDA–ODA films cured at 250 and 300 °C. m was allowed to vary, and it was found that the best fits were obtained when $m = 1 \pm 0.2$. This is a simple Lorentzian profile plus a linear background,

$$qI(q) = a + b(q - q_0) + \frac{2}{\pi\Delta q}\frac{I_0}{1 + 4\left(\frac{q - q_0}{\Delta q}\right)^2} \quad \text{(B-3)}$$

where I_0 is the area under the curve, q_0 is the position of the reflection, and Δq is the FWHM. Since the Lorentzian curve has broad tails, the fitted I_0 overestimates the observed scattering. Therefore, the integrated intensity, I_{int}, was determined by integrating the Lorentzian profile from 0.3 to 0.6 Å^{-1} and is given by

$$I_{int} = \frac{I_0}{\pi}\left(\arctan\left(\frac{B - q_0}{\Delta q}\right) + \arctan\left(\frac{q_0 - A}{\Delta q}\right)\right) \quad \text{(B-4)}$$

where $A = 0.3$ Å^{-1} and $B = 0.6$ Å^{-1}. This allows the integrated intensity to be self-consistently compared to that from other functional forms. Furthermore, the broad tails to the Lorentzian also cause the fitted FWHM to be about 11% larger than the FWHM obtained visually. The FWHM discussed in the test are the fitted ones.

Lorentzian Profile Raised to the 6.7 Power. For the (002) reflection of the films cured at 420 °C, eq B-1 fits best when $m = 6.7 \pm 1$. The fitting function is given by

$$qI(q) = a + b(q - q_0) + \frac{2}{\pi\Delta q}\frac{1.425I_{int}}{\pi\Delta q\left(1 + 4\left(\frac{q - q_0}{3.03\Delta q}\right)^2\right)^{6.7}} \quad \text{(B-5)}$$

where I_{int} is the integrated intensity and Δq is the FWHM. The constants $A = 1.425$ and $B = 3.03$ were calculated for $m = 6.7$. No cutoff of the integrated intensity was necessary since the contribution of the tails was small. Because the (002) reflection is not symmetric, a second L6.7 function was also included to provide a good phenomenological fit to the asymmetry. This contribution was fixed between 0.48 and 0.49 Å^{-1}, and for the p-PAE cured at 420 °C, the ratio of the intensities of the second contribution to the first is about 3%.

Gaussian Profile. For convenience, the Gaussian profile was used to fit the (004), (101), and (201) reflections of PMDA–ODA. For these reflections, the data were in general too noisy to accurately fit a value for m in eq B-1. The form of the Gaussian profile is

$$qI(q) = a + b(q - q_0) + \frac{2}{\Delta q}I_{int}\sqrt{\frac{\ln 2}{\pi}}\exp\left[-4\ln 2\left(\frac{q - q_0}{\Delta q}\right)^2\right] \quad \text{(B-6)}$$

where I_{int} is the integrated intensity and Δq is the FWHM.

Appendix C

Paracrystallinity. In the paracrystalline model, the scattering is characterized by a normalized probability function describing the distance between near neighbor atoms on a one-dimensional lattice. For a narrow distribution of near neighbor separation distances, the scattering will contain multiple orders of reflection, although the order is not truly long range unless the distribution function is a δ function.

When the breadth of the distribution is small, the line width is given by[32,38]

$$\Delta q_{para} = \frac{2\pi}{d}(\pi g m)^2 \quad \text{(C-1)}$$

where d is the average near neighbor distance, m is the reflection order, and g is a measure of the paracrystalline distortion which is defined to be the mean square positional fluctuation divided by d. Since $m = qd/2\pi$, then[40]

$$\Delta q_{para} = \frac{1}{2}\pi d g^2 q^2 \quad \text{(C-2)}$$

Assuming Gaussian line shapes, Δq_{para} is added in quadrature to the broadening from finite size.

The line width is proportional to q^2 in the paracrystalline model, while it is proportional to q for inhomogeneous strain and is constant for finite domain sizes. Therefore, paracrystallinity can be differentiated from strain and domain size by examining the widths of higher order reflections. If only two reflections are present, it is not possible to distinguish among strain broadening, paracrystalline disorder, or domain size.

In the paracrystalline model, the positions of higher order reflections are generally not integral multiples of the position of the first order reflection. The shift in the second order reflection is dependent on the shape of the distribution function of the nearest neighbor separation distances.[41,42] Distribution functions which cause the ratio of the positions of the first and second order peaks to be less than 2 are termed *negatively skewed*. Likewise, *positively skewed* distributions yield a ratio greater than 2.

References and Notes

(1) Theodorou, D. N. *Macromolecules* **1988**, *21*, 1391.
(2) Kumar, S. K.; Vacatello, M.; Yoon, D. Y. *Macromolecules* **1990**, *23*, 2189.
(3) Bitsanis, I.; Hadziioannou, G. *J. Chem. Phys.* **1990**, *92*, 3827.
(4) See for example: *Surface X-ray and Neutron Scattering*; Zabel, H., Robinson, I. K., Eds.; Springer-Verlag: New York, 1992.
(5) Martin, D. C.; Berger, L. L.; Gardner, K. H. *Macromolecules* **1991**, *24*, 3921.
(6) Russell, T. P. *Mater. Sci. Rep.* **1990**, *5*, 171.
(7) Stamm, M. *Adv. Polym. Phys.* **1991**, *100*, 1.
(8) Bhatia, Q. S.; Pan, D. H.; Koberstein, J. T. *Macromolecules* **1988**, *21*, 2166.
(9) Coulon, G.; Russell, T. P.; Deline, V. R.; Green, P. F. *Macromolecules* **1989**, *22*, 2581.
(10) Bloch, J. M.; Sansone, M.; Rondelez, F.; Peiffer, D. G.; Pincus, P.; Kim, M. W.; Eisenberger, P. M. *Phys. Rev. Lett.* **1985**, *54*, 1039.
(11) Green, P. F.; Doyle, B. L. In *New Characterization Techniques for Thin Polymer Films*; Tony, H., Nguyen, L. T., Eds.; Wiley: New York, 1990.
(12) Eisenberger, P.; Marra, W. C. *Phys. Rev. Lett.* **1981**, *16*, 1081.
(13) Huang, K. G.; Gibbs, D.; Zehner, D. M.; Sandy, A. R.; Mochrie, S. G. J. *Phys. Rev. Lett.* **1990**, *65*, 3313.
(14) Thomas, B. N.; Barton, S. W.; Novak, F.; Rice, S. A. *J. Chem. Phys.* **1987**, *86*, 1036.
(15) Toney, M. F.; Huang, T. C.; Brennan, S.; Rek, Z. *J. Mater. Res.* **1988**, *3*, 351.
(16) Dosch, H.; Mailaender, L.; Lied, A.; Peisl, J.; Grey, F.; Johnson, R. L.; Krummacher, S. *Phys. Rev. Lett.* **1988**, *60*, 2382.
(17) Mailaender, L.; Dosch, H.; Peisl, J.; Johnson, R. L. *Phys. Rev. Lett.* **1990**, *64*, 2527.
(18) Factor, B. J.; Russell, T. P.; Toney, M. F. *Phys. Rev. Lett.* **1991**, *66*, 1181.
(19) Factor, B. J. Ph.D. Thesis, Stanford University, 1992; Factor, B. J.; Russell, T. P.; Toney, M. F. *Macromolecules*, submitted.

(20) Volksen, W.; Yoon, D. Y.; Hedrick, J. L.; Hofer, D. C. Materials Science of High Temperature Polymers for Microelectronics. In *Materials Research Society Symposia Proceedings*; Geubb, G. F., Mita, I., Yoon, D. Y., Eds.; Elsevier: New York, **1991**; Vol. 227, p 23.
(21) Stephenson, G. B. *Nucl. Instrum. Methods Phys. Res.* **1988**, *A266*, 447.
(22) Lekner, J. *Theory of Reflection*; Martinus Nijhoff Publishers: Dordrecht, The Netherlands, 1987.
(23) Vineyard, G. H. *Phys. Rev. B* **1982**, *26*, 4146.
(24) Born, M.; Wolfe, E. *Principles of Optics*; Pergammon Press: Oxford, U.K., 1985.
(25) Becker, R. S.; Golevechenko, J. A.; Patel, J. R. *Phys. Rev. Lett.* **1983**, *50*, 153.
(26) Busing, W. R.; Levy, H. A. *Acta Crystallogr.* **1967**, *22*, 457.
(27) Warren, B. E. *X-ray Diffraction*; Addison-Wesley: Reading, PA, 1969.
(28) Russell, T. P.; Gugger, H.; Swalen, J. D. *J. Polym. Sci.; Polym. Phys. Ed.* **1983**, *21*, 1745.
(29) Takahashi, N.; Yoon, D. Y.; Parrish, W. *Macromolecules* **1984**, *17*, 2583.
(30) Kazaryan, L. G.; Tsvankin, D. Y.; Ginzburg, B. M.; Tuichiev, S.; Korzhavin, L. N.; Frenkel, S. Y. *Vysokoml. Soedin.* **1972**, *A14*, 1199; *Polym. Sci. USSR (Engl. Transl.)* **1979**, *21*, 1644.
(31) Alexander, L. E. *X-ray Diffraction Methods in Polymer Science*; John Wiley and Sons: New York, 1969.
(32) Kakudo, M.; Kasai, N. *X-ray Diffraction by Polymers*; Kodansha Ltd.: Tokyo, 1972.
(33) Hosemann, R.; Bagchi, S. N. *Direct Analysis of Diffraction by Matter*; North Holland: Amsterdam, 1962.
(34) Scherrer, P. *Nachr. Goettingen Ges.* **1918**, *2*, 8.
(35) Warren, B. E.; Averbach, B. L. *J. Appl. Phys.* **1950**, *21*, 595.
(36) Cotts, P. M.; Volksen, W. *Polym. News* **1990**, *15*, 106.
(37) Russell, T. P. *J. Polym. Sci., Polym. Phys. Ed.* **1984**, *22*, 1105.
(38) Wilson, A. J. C. *X-ray Optics*; Methuen: London, 1949.
(39) Toney, M. F.; Brennan, S. *J. Appl. Phys.* **1989**, *66*, 1861.
(40) Bonart, R.; Hosemann, R.; McCullough, R. L. *Polymer* **1963**, *4*, 199.
(41) Crist, B. *J. Polym. Sci., Polym. Phys. Ed.* **1973**, *11*, 635.
(42) Crist, B.; Morosoff, N. *J. Polym. Sci., Polym. Phys. Ed.* **1973**, *11*, 642.
(43) Gattiglia, E.; Russell, T. P. *J. Polym. Sci., Polym. Phys. Ed.* **1989**, *27*, 2131.